



# MoBGS: Motion Deblurring Dynamic 3D Gaussian Splatting for Blurry Monocular Video

Minh-Quan Viet Bui<sup>1\*</sup> Jongmin Park<sup>1\*</sup> Juan Luis Gonzalez Bello<sup>1</sup> Jaeho Moon<sup>1</sup>  
 Jihyong Oh<sup>2†</sup> Munchurl Kim<sup>1†</sup>

<sup>1</sup>KAIST <sup>2</sup>Department of Imaging Science, GSAIM, Chung-Ang University

{bvmquan, jm.park, juanluisgb, jaeho.moon, mkimee}@kaist.ac.kr jihyongoh@cau.ac.kr  
<https://kaist-viclab.github.io/mobgs-site/>

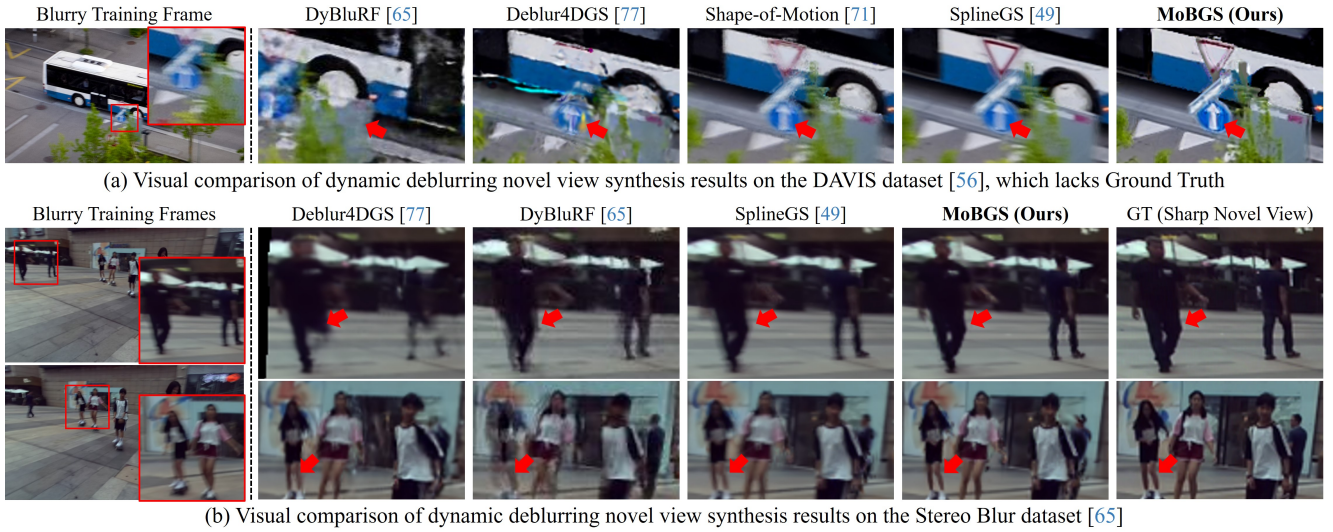


Figure 1. Our MoBGS achieves state-of-the-art dynamic deblurring novel view synthesis on both (a) casually captured real-world blurry monocular videos [56] and (b) synthesized blurry monocular videos [65]. For a clearer comparison, each region is cropped and enlarged.

## Abstract

We present MoBGS, a novel deblurring dynamic 3D Gaussian Splatting (3DGS) framework capable of reconstructing sharp and high-quality novel spatio-temporal views from blurry monocular videos in an end-to-end manner. Existing dynamic novel view synthesis (NVS) methods are highly sensitive to motion blur in casually captured videos, resulting in significant degradation of rendering quality. While recent approaches address motion-blurred inputs for NVS, they primarily focus on static scene reconstruction and lack dedicated motion modeling for dynamic objects. To overcome these limitations, our MoBGS introduces a novel Blur-adaptive Latent Camera Estimation (BLCE) method for effective latent camera trajectory estimation, improving global camera motion deblurring. In addition, we propose a physically-inspired Latent Camera-induced Exposure Estimation (LCEE) method to ensure consistent deblurring of

both global camera and local object motion. Our MoBGS framework ensures the temporal consistency of unseen latent timestamps and robust motion decomposition of static and dynamic regions. Extensive experiments on the Stereo Blur dataset and real-world blurry videos show that our MoBGS significantly outperforms the very recent advanced methods (DyBluRF and Deblur4DGS), achieving state-of-the-art performance for dynamic NVS under motion blur.

## 1. Introduction

Novel View Synthesis (NVS) has seen significant advancements in recent years, with applications spanning Virtual Reality (VR), Augmented Reality (AR), and film production. While dynamic NVS methods [3, 4, 6, 12, 18, 20, 21,

\*Co-first authors (equal contribution).

†Co-corresponding authors.

31, 33–35, 47, 49, 52, 57, 59, 66, 69, 71, 73, 75, 81] have made substantial progress in reconstructing realistic scenes from monocular videos and multi-camera setups, their performance remains highly dependent on the quality of input observations. In particular, motion blur, which frequently occurs in casually captured videos due to fast-moving objects [48, 84] or camera shake [5, 83], poses a major challenge. Since NVS techniques rely on the precise reconstruction of scene geometry and appearance, the loss of sharp details caused by blur can severely degrade the temporal consistency and fidelity of the synthesized novel views.

To reconstruct sharp 3D scenes from blurry observations, several deblurring NVS methods [7, 24–28, 43, 54, 65, 70, 77, 86] have been developed recently based on estimating latent camera poses during the exposure time. Most of these methods focus only on static scene deblurring, without considering that object motion also occurs during the same exposure time along with camera movement, making them less effective for dynamic scenes with complex object motions. Only a few methods [7, 65, 77] have been explored for dynamic deblurring NVS from blurry monocular videos. However, there are several limitations with these methods [7, 65, 77]. First of all, none of these methods thoroughly estimate the exposure time while considering both global camera motion and local object motion, even though accurate exposure time estimation is a key factor in achieving effective motion deblurring for dynamic NVS. Incorrect exposure time estimation can lead to inconsistent and ineffective deblurring, particularly in dynamic regions where motion varies significantly. DyBluRF [65] (Sun *et al.*, 2024) simply assumes the exposure time to be the interval between adjacent frames, which can lead to excessively large blur estimations for moving objects. Deblur4DGS [77] independently predicts the exposure time as a learnable parameter, without any constraint related to global camera motion, even though both camera and object motions contribute to the blurriness during the same exposure time. DyBluRF [7] (Bui *et al.*, 2023) does not estimate the exposure time at all. Second, DyBluRF [65] and Deblur4DGS [77] directly adopt pre-computed motion masks to decompose static and dynamic regions. However, motion masks obtained from blurry frames are inaccurate, as blurriness hinders off-the-shelf motion segmentation networks [34, 35, 39, 71] from producing clean boundaries around moving objects. Third, NeRF-based methods [7, 65] require extensive computational resources and long training times, limiting their practicality for real-world applications. Lastly, none of these methods demonstrate their deblurring NVS performance on real-world blurry videos captured in casual settings.

To address these limitations and achieve high-quality, sharp novel view synthesis from diverse blurry monocular videos, we propose MoBGS, a novel dynamic deblur-

ring NVS method based on 3D Gaussian Splatting [23]. To effectively handle the blurriness caused by both global camera motion and local object motion in blurry monocular videos, our MoBGS first accurately predicts latent camera poses for each blurry frame by considering the corresponding blurriness using our Blur-adaptive Latent Camera Estimation (BLCE) method. Then, based on these latent camera poses, our MoBGS estimates the corresponding exposure time via our novel Latent Camera-induced Exposure Estimation (LCEE) method. The estimated exposure time is then used to model the blurriness of moving objects while ensuring that the blurriness caused by both global camera motion and local object motion occurs within the same exposure period. Moreover, we incorporate two regularization losses to enhance the temporal consistency of dynamic objects and to refine pre-computed motion masks for accurate scene decomposition. Extensive quantitative and qualitative evaluations on the Stereo Blur dataset [65] and real-world captured videos [56] demonstrate that our MoBGS substantially outperforms recent state-of-the-art (SOTA) methods in dynamic deblurring NVS quality. In summary, our main contributions are as follows:

- We introduce MoBGS, a novel motion deblurring framework for dynamic 3D Gaussian Splatting (3DGS) that effectively reconstructs high-quality spatio-temporal novel views from various blurry monocular videos.
- A *Blur-adaptive Latent Camera Estimation* (BLCE) method is proposed to accurately estimate latent camera trajectories, considering the blurriness of video frames.
- A *Latent Camera-induced Exposure Estimation* (LCEE) method is proposed to infer latent exposure timestamps, ensuring consistent deblurring by aligning global camera motion and local object motion.
- Our MoBGS framework is extensively evaluated on the Stereo Blur dataset [65] and real-world blurry video sequences [56], demonstrating significant improvements over SOTA methods in both reconstruction quality and temporal consistency.

## 2. Related Work

### 2.1. Dynamic Novel View Synthesis

Following the success of NeRF [44] in novel view synthesis (NVS) for static scenes, various methods have been developed to tackle the challenges of dynamic NVS. To model scene dynamics from videos, these approaches leverage canonical fields [2, 17, 22, 39, 50, 51, 57, 62, 66, 74, 80], scene flows [15, 19, 34, 35], spatio-temporal radiance fields [33, 68, 78], and grid-based architectures [3, 8, 18, 59]. More recently, 3DGS [23]-based methods [11, 16, 21, 29–31, 36, 37, 40, 63, 71, 76, 81] have been proposed to achieve faster and higher-fidelity dynamic NVS. D3DGS

[81] predicts the offsets of attributes of 3D Gaussians for each time using an MLP network. 4DGS [76] exploits multiple voxel planes as spatio-temporal structure encoders to model deformations of 3D Gaussians across time. E-D3DGS [4] introduces per-Gaussian and temporal embeddings to model Gaussian deformations, enabling more accurate reconstruction in complex dynamic scenes. Shape-of-Motion [71] utilizes rigid transformations to model the time-varying means and rotations of 3D Gaussians with globally shared bases and per-Gaussian motion coefficients. SplineGS [49] employs motion-adaptive functions based on the cubic Hermite spline function [1, 13] to represent the smooth and continuous trajectories of 3D Gaussians across time. However, none of these methods is designed for sharp scene reconstruction from blurry monocular training videos. As a result, their rendering outputs still exhibit blurriness for the blurry monocular input videos.

## 2.2. Deblurring Novel View Synthesis

A variety of deblurring NVS methods [24–26, 28, 43, 53, 54, 70, 86] have been developed to generate sharp renderings while preserving consistent 3D geometry from blurry images. DeblurNeRF [43] is a pioneering work for deblurring NVS that predicts a spatial blur kernel for each input ray to model blurriness. BAD-NeRF [70] estimates virtual camera trajectories during exposure time using a bundle adjustment formulation and averages the renderings to synthesize blurry images. Deblurring 3DGS [24] is the first 3DGS-based deblurring NVS method which uses a shallow MLP that transforms 3D Gaussians to model blurriness. BAD-GS [86] builds upon the work [70] by incorporating 3D Gaussian representations, further enhancing rendering quality and efficiency. However, none of these methods are well-suited for dynamic scenes, as they lack motion-aware deblurring in the temporal dimension. For this, several dynamic deblurring NVS methods [41, 42, 65, 77] have been proposed to handle the blurriness caused by both camera and object motions from blurry monocular videos. DyBluRF [65] utilizes the Discrete Cosine Transform (DCT) [67] to model the time-dependent trajectories of 3D points to enforce temporal consistency. However, this method suffers from long training times and a limited representation capacity, which are inherent limitations of NeRF [44]-based architectures. Very recently, Deblur4DGS [77] proposes a 3DGS [23]-based method built on the deformation model of Shape-of-Motion [71]. This method estimates the exposure time as a learnable parameter for each frame, with no constraint related to global camera motion. In contrast, our MoBGS estimates the exposure time by considering both camera and object motions, achieving more robust and precise blur modeling than the existing methods [65, 77].

## 3. Preliminaries

**3D Gaussian Splatting.** 3DGS [23] represents 3D scenes explicitly by leveraging anisotropic 3D Gaussians. Each 3D Gaussian is defined by a mean  $\mu \in \mathbb{R}^3$  and a covariance matrix  $\Sigma \in \mathbb{R}^{3 \times 3}$  as

$$G(\mathbf{x}) = e^{-\frac{1}{2}(\mathbf{x}-\mu)^\top \Sigma^{-1}(\mathbf{x}-\mu)}, \text{ where } \Sigma = \mathbf{R} \mathbf{S} \mathbf{S}^\top \mathbf{R}^\top, \quad (1)$$

where  $\mathbf{S} \in \mathbb{R}^{3 \times 3}$  and  $\mathbf{R} \in \mathbb{R}^{3 \times 3}$  denote the scaling and rotation matrices of the 3D Gaussian, respectively. To project each 3D Gaussian onto 2D domain for rendering, a 2D covariance matrix  $\Sigma' \in \mathbb{R}^{2 \times 2}$  is computed as  $\Sigma' = \mathbf{J} \mathbf{W} \Sigma \mathbf{W}^\top \mathbf{J}^\top$ , where  $\mathbf{J}$  is the Jacobian of the affine approximation of the projective transformation [87] and  $\mathbf{W}$  is a viewing transformation matrix. The rendered color  $\mathbf{C}(\mathbf{u})$  at 2D pixel location  $\mathbf{u}$  is computed by blending  $\mathcal{N}$  depth-ordered 3D Gaussians overlapped at  $\mathbf{u}$  as

$$\mathbf{C}(\mathbf{u}) = \sum_{i \in \mathcal{N}} c_i \alpha_i \prod_{j=1}^{i-1} (1 - \alpha_j), \quad (2)$$

where  $c_i$  and  $\alpha_i$  are the color and the density of the  $i^{\text{th}}$  3D Gaussian, respectively, computed using learnable spherical harmonic (SH) coefficients  $\mathcal{C} \in \mathbb{R}^k$  and an opacity  $\sigma \in \mathbb{R}$ .

**Spline-based 3D Gaussian Deformation.** To model dynamic scenes, SplineGS [49] represents each scene with a combination of static 3D Gaussians  $\{G_i^{\text{st}}\}_{i \in [1, n^{\text{st}}]}$  for the stationary background and dynamic 3D Gaussians  $\{G_i^{\text{dy}}\}_{i \in [1, n^{\text{dy}}]}$  for moving objects. To represent the smooth and continuous deformation of each dynamic Gaussian over time, SplineGS [49] utilizes a set of  $N_c$  learnable control points  $\mathbf{P} = \{\mathbf{p}_n \in \mathbb{R}^3\}_{n \in [1, N_c]}$  as an additional attribute, where the time-varying mean  $\mu(t)$  at time  $t$  for each dynamic Gaussian is formulated as  $\mu(t) = S(t, \mathbf{P})$  that is specifically expressed as:

$$\begin{aligned} S(t, \mathbf{P}) = & (2t_r^3 - 3t_r^2 + 1)\mathbf{p}_{\lfloor t_s \rfloor} + (t_r^3 - 2t_r^2 + t_r)\mathbf{m}_{\lfloor t_s \rfloor} \\ & + (-2t_r^3 + 3t_r^2)\mathbf{p}_{\lfloor t_s \rfloor + 1} + (t_r^3 - t_r^2)\mathbf{m}_{\lfloor t_s \rfloor + 1}, \quad (3) \\ t_r = & t_s - \lfloor t_s \rfloor, \quad t_s = t_n(N_c - 1), \quad t_n = t/(N_f - 1), \end{aligned}$$

where  $\mathbf{m}_n$  denotes the approximated tangent at the control point  $\mathbf{p}_n$ , computed as  $\mathbf{m}_n = \frac{\mathbf{p}_{n+1} - \mathbf{p}_{n-1}}{2}$ .  $N_f$  is the total number of training video frames. We adopt this spline-based deformation for dynamic 3D Gaussians to accurately capture the motion trajectories of moving objects and to effectively model the blurriness across the exposure time.

**Motion Blur Formulation.** As in previous works [25, 42, 65, 70, 77, 86], a motion-blurred image  $\mathbf{B} \in \mathbb{R}^{H \times W \times 3}$  can be expressed as the integration of latent sharp images  $\mathbf{C}_\varphi \in \mathbb{R}^{H \times W \times 3}$  captured over an exposure time  $\mathcal{T}$  as

$$\mathbf{B} = g \int_0^\mathcal{T} \mathbf{C}_\varphi d\varphi, \quad (4)$$

where  $g$  is a normalization factor and  $\varphi$  is an infinitesimal time interval. This process is commonly approximated by



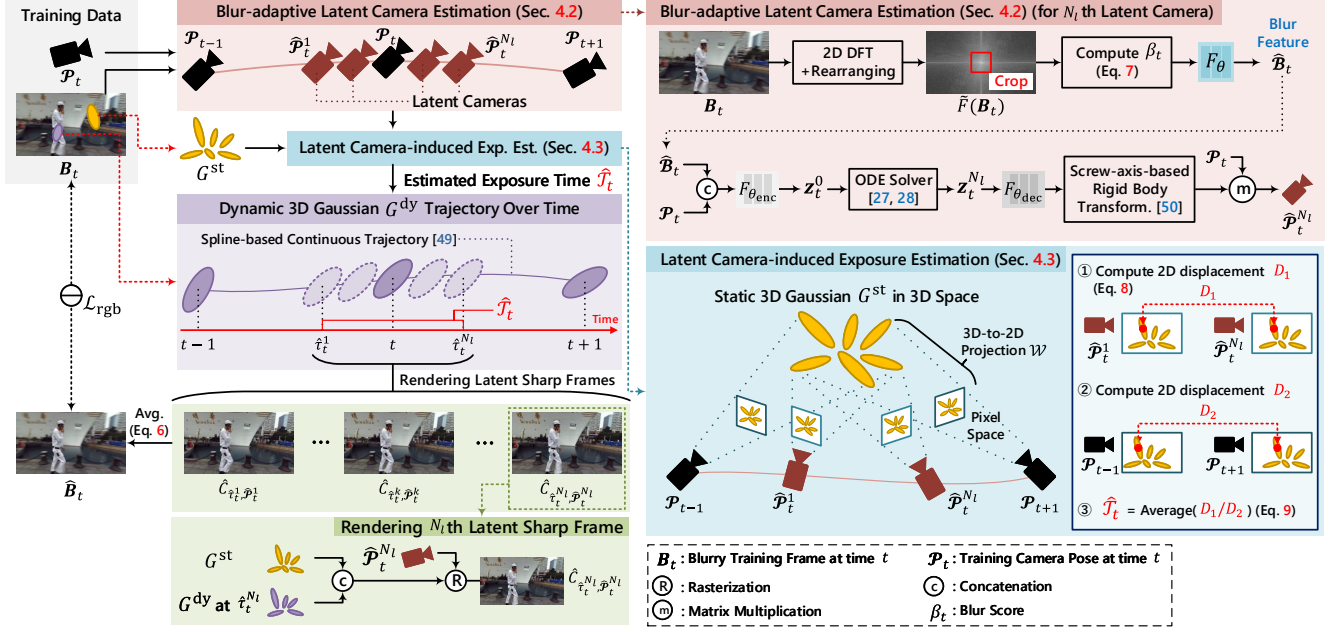


Figure 2. **Overview of MoBGS.** To achieve high-quality dynamic deblurring NVS, MoBGS accurately models scene blurriness by jointly considering global camera and local object motion over the same exposure time. It first estimates latent camera poses for each blurry frame using our Blur-adaptive Latent Camera Estimation (BLCE) method. Then, leveraging these latent camera poses, it estimates the corresponding exposure time via our Latent Camera-induced Exposure Estimation (LCEE) method, ensuring a physically consistent blur modeling of local moving objects.

averaging  $N_l$  latent sharp images, each denoted by  $C_{\tau^k}$ , sampled at a discrete timestamp  $\tau^k$  within  $\mathcal{T}$  as

$$B \approx \frac{1}{N_l} \sum_{k=1}^{N_l} C_{\tau^k}. \quad (5)$$

## 4. Proposed Method: MoBGS

### 4.1. Overview of MoBGS

Fig. 2 illustrates the overall framework of our MoBGS. Given a set of blurry monocular video frames  $\{B_t\}_{t \in [1, N_f]}$  with camera poses  $\{\mathcal{P}_t \in \mathbb{R}^{4 \times 4}\}_{t \in [1, N_f]}$  and a shared camera intrinsic matrix  $K \in \mathbb{R}^{3 \times 3}$ , MoBGS aims to synthesize sharp novel views by accurately modeling scene blurriness caused by both global camera and local object (GCLO) motion. The core principle of our blur modeling is that the blurriness of both the static background and moving objects occurs over the same exposure time for each blurry video frame. Based on this fundamental principle, to handle the blurriness of the static background caused by global camera motion, we first estimate a set of  $N_l$  latent camera poses  $\{\hat{\mathcal{P}}_t^k\}_{k \in [1, N_l]}$  for each input blurry frame  $B_t$  using our Blur-adaptive Latent Camera Estimation (BLCE) method (Sec. 4.2). These estimated latent camera poses are then used to compute the exposure time  $\hat{\mathcal{T}}_t$  for each blurry frame through our Latent Camera-induced Exposure Estimation (LCEE) method (Sec. 4.3). To model the spatially-varying blur caused by local object motion, we leverage the

timestamps  $\{\hat{\tau}_t^k\}_{k \in [1, N_l]}$  sampled within the computed exposure time  $\hat{\mathcal{T}}_t$  to predict the corresponding object motion, enabling fine-grained modeling of local object motion blur. Finally, we render each latent sharp frame at a sampled latent timestamp and its corresponding latent camera pose. We denote as  $\hat{C}_{\tau, \mathcal{P}}$  the rendered latent sharp frame at a latent timestamp  $\tau$  with a camera pose  $\mathcal{P}$ . Then our final blurry frame prediction is formulated as (similar to Eq. 5)

$$\hat{B}_t = \frac{1}{N_l} \sum_{k=1}^{N_l} \hat{C}_{\hat{\tau}_t^k, \hat{\mathcal{P}}_t^k}, \quad \hat{\tau}_t^k = t + \hat{\mathcal{T}}_t \frac{k - \lceil \frac{N_l}{2} \rceil}{N_l}, \quad (6)$$

where  $\lceil \cdot \rceil$  denotes the rounding up operation. In addition, we adopt an unsupervised, optical flow-based reprojection loss  $\mathcal{L}_{\text{tr}}$  to enhance the temporal consistency of latent renderings. We also adopt an unsupervised mask loss,  $\mathcal{L}_{\text{umd}}$ , which constrains the density  $\alpha$  of each dynamic 3D Gaussian toward enhancing the robustness of static and dynamic scene decomposition (Sec. 4.4).

### 4.2. Blur-adaptive Latent Camera Estimation

To address the blurriness caused by global camera motion, we propose the BLCE method, which estimates a continuous latent camera trajectory based on the blur intensity of each frame. The estimated trajectory is strongly influenced by the degree of blur, with a more severe blurriness resulting in longer and more complex trajectories. To compute the blur intensity of each frame, we exploit the fact



that blurry frames typically contain a higher proportion of low-frequency components [38, 60, 61, 79]. Based on this observation, we define the blur score as the ratio of the magnitudes within the low-frequency region to the total magnitudes in the frequency spectrum of the frame. We first apply a 2D Discrete Fourier Transform (DFT) to  $B_t$ , then rearrange the resulting DFT coefficients to center the low-frequency components, producing the shifted DFT  $\tilde{\mathcal{F}}(B_t)$ . The blur score  $\beta_t$  can then be expressed as

$$\beta_t = \frac{\sum_{\xi \in \Lambda} M_t(\xi)}{\sum_{\xi} M_t(\xi)}, \quad \text{where } M_t = |\tilde{\mathcal{F}}(B_t)| \quad (7)$$

where  $\xi$  denotes a 2D frequency index and  $\Lambda$  denotes the center-cropped square region with a side length of  $s$ , which covers the low-frequency components in  $\tilde{\mathcal{F}}(B_t)$ . A blur feature  $\mathcal{B}_t$  is extracted from  $\beta_t$  as  $\mathcal{B}_t = F_\theta(\phi(\beta_t))$ , where  $F_\theta$  is a blur feature encoder that is a shallow MLP network and  $\phi(\cdot)$  denotes the positional encoding [44]. We use the blur feature  $\mathcal{B}_t$  along with the corresponding camera pose  $\mathcal{P}_t$  to predict latent camera poses  $\{\hat{\mathcal{P}}_t^k\}_{k \in [1, N_t]}$  along a smooth trajectory. Specifically, we encode a latent vector  $\mathbf{z}_t^0$  using a shallow MLP network  $F_{\text{enc}}$ , as  $\mathbf{z}_t^0 = F_{\text{enc}}([\mathcal{B}_t, \mathcal{P}_t])$ , where  $[\cdot, \cdot]$  denotes concatenation. We then predict a series of  $N_t$ -ordered latent vectors  $\{\mathbf{z}_t^k\}_{k \in [1, N_t]}$  from  $\mathbf{z}_t^0$  using a Neural-ODE solver [9], following a similar approach to [27, 28]. Each  $\mathbf{z}_t^k$  is used to predict a learnable screw axis  $(\omega_t^k; \mathbf{v}_t^k) \in \mathbb{R}^6$  via a decoder  $F_{\text{dec}}$ , as  $(\omega_t^k; \mathbf{v}_t^k) = F_{\text{dec}}(\mathbf{z}_t^k)$ . Finally, each latent camera pose  $\hat{\mathcal{P}}_t^k$  is computed by applying a residual transformation  $\Psi(\omega_t^k, \mathbf{v}_t^k)$  to the initial camera pose  $\mathcal{P}_t$ , as  $\hat{\mathcal{P}}_t^k = \mathcal{P}_t \Psi(\omega_t^k, \mathbf{v}_t^k)$ , where  $\Psi(\cdot)$  denotes the screw-axis-based rigid body transformation from [50].

### 4.3. Latent Camera-induced Exposure Estimation

Unlike previous methods for dynamic deblurring NVS [65, 77], which model  $\hat{\mathcal{T}}_t$  as either a fixed constant or a learnable parameter with a high degree of freedom, we propose the LCEE method to constrain  $\hat{\mathcal{T}}_t$  using the predicted latent camera trajectories obtained by the BLCE (Sec. 4.2). The LCEE ensures greater consistency between the deblurring processes applied to static backgrounds and moving objects, enabling more robust motion deblurring for dynamic objects. Let  $\mathcal{W}(\mathcal{P}, \mathbf{x})$  be a projection function that maps a 3D position  $\mathbf{x}$  to a pixel coordinate  $\mathbf{u}$  under a given camera pose  $\mathcal{P}$ . Given the estimated latent camera poses  $\{\hat{\mathcal{P}}_t^k\}_{k \in [1, N_t]}$  corresponding to each blurry frame  $B_t$ , we select the first and last latent camera poses,  $\hat{\mathcal{P}}_t^1$  and  $\hat{\mathcal{P}}_t^{N_t}$ . As shown in Fig. 2, we then compute the 2D displacement between the two projections of each static 3D Gaussian’s mean  $\mu_i^{\text{st}}$  for the two selected latent camera poses,  $\hat{\mathcal{P}}_t^1$  and  $\hat{\mathcal{P}}_t^{N_t}$ , as

$$D(\hat{\mathcal{P}}_t^1, \hat{\mathcal{P}}_t^{N_t}, \mu_i^{\text{st}}) = \|\mathcal{W}(\hat{\mathcal{P}}_t^1, \mu_i^{\text{st}}) - \mathcal{W}(\hat{\mathcal{P}}_t^{N_t}, \mu_i^{\text{st}})\|_2. \quad (8)$$

This 2D displacement quantifies the extent to which the static 3D Gaussian shifts across the image plane due to global camera motion between the first and last latent camera poses over the exposure time. Similarly, as shown in Fig. 2, we compute the 2D displacement between the two projections of the mean  $\mu_i^{\text{st}}$  for the *training* camera poses  $\mathcal{P}_{t-1}$  and  $\mathcal{P}_{t+1}$ , representing the displacement over the interval from  $t-1$  to  $t+1$ , denoted as  $D(\mathcal{P}_{t-1}, \mathcal{P}_{t+1}, \mu_i^{\text{st}})$ . To estimate the per-frame exposure time  $\hat{\mathcal{T}}_t$ , we compute the average ratio between the two 2D displacements as

$$\hat{\mathcal{T}}_t = \frac{1}{n^{\text{st}}} \sum_{i=1}^{n^{\text{st}}} \frac{D(\hat{\mathcal{P}}_t^1, \hat{\mathcal{P}}_t^{N_t}, \mu_i^{\text{st}}) + \epsilon}{D(\mathcal{P}_{t-1}, \mathcal{P}_{t+1}, \mu_i^{\text{st}}) + \epsilon}, \quad (9)$$

where  $n^{\text{st}}$  is the number of static 3D Gaussians and  $\epsilon$  is a smoothing term to avoid numerical issues. As shown in Eq. 6, the estimated exposure time  $\hat{\mathcal{T}}_t$  is used to compute the latent timestamps  $\hat{\tau}_t^k$ . Then, each latent sharp frame  $\hat{\mathcal{C}}_{\hat{\tau}_t^k, \hat{\mathcal{P}}_t^k}$  at each latent timestamp  $\hat{\tau}_t^k$  is independently rendered using the static  $\{G_i^{\text{st}}\}_{i \in [1, n^{\text{st}}]}$  and dynamic 3D Gaussians  $\{G_i^{\text{dy}}\}_{i \in [1, n^{\text{dy}}]}$ . Finally, the rendered blurry frame  $\hat{B}_t$  is obtained by averaging these latent sharp frames.

### 4.4. Optimization

To enhance deblurring dynamic NVS performance, we adopt two regularization losses and modify them for stable optimization of our MoBGS, aiming to achieve robust scene decomposition and improved temporal consistency.

**Unsupervised Motion Decomposition Loss ( $\mathcal{L}_{\text{umd}}$ ).** To improve the representation capacity of dynamic scenes, recent dynamic NVS methods [19, 34, 35, 39, 71], including dynamic deblurring NVS methods [7, 77], require pre-computed motion masks to decompose static and dynamic 3D Gaussians. However, accurately obtaining motion masks from blurry video frames is challenging, as off-the-shelf models [34, 39, 71] often fail to consistently generate reliable segmentation masks for moving objects. To overcome this issue, we adopt an unsupervised motion decomposition loss  $\mathcal{L}_{\text{umd}}$  which was proposed in NeRF-based method [7], and modify it to encourage the densities  $\alpha^{\text{dy}}$  of dynamic 3D Gaussians to converge towards either 0 or 1, thereby promoting a clear decomposition between static and dynamic regions.  $\mathcal{L}_{\text{umd}}$  is formulated as

$$\mathcal{L}_{\text{umd}} = \sum_{i=1}^{n^{\text{dy}}} -\alpha_i^{\text{dy}} \log \alpha_i^{\text{dy}} - \bar{\alpha}_i^{\text{dy}} \log \bar{\alpha}_i^{\text{dy}} + (\alpha_i^{\text{dy}})^2, \quad (10)$$

where  $\bar{\alpha}_i^{\text{dy}} = 1 - \alpha_i^{\text{dy}}$ . The first two terms promote binary regularization by minimizing entropy, while the last term encourages sparsity, ensuring that only necessary 3D Gaussians are classified as dynamic, reducing the risk of over-segmentation in dynamic regions of blurry video frames.

**Temporal Consistency Reprojection Loss ( $\mathcal{L}_{\text{ter}}$ ).** Inspired by the cycle rendering consistency techniques from

NeRF-based methods [34, 35], we adopt a temporal consistency reprojection loss,  $\mathcal{L}_{\text{tcr}}$ , to preserve better motion coherence between the rendered latent sharp frames  $\{\hat{C}_{\tau_t^k, \mathcal{P}_t}^k\}_{k \in [1, N_t]}$ .  $\mathcal{L}_{\text{tcr}}$  penalizes texture inconsistencies in rendered latent sharp frames, thereby enhancing the temporal consistency of  $\{G_i^{\text{dy}}\}_{i \in [1, n^{\text{dy}}]}$  while simultaneously propagating sharp details over the exposure time.  $\mathcal{L}_{\text{tcr}}$  for the target time  $t$  is formulated as

$$\mathcal{L}_{\text{tcr}} = \sum_{k=1}^{N_t} |\hat{C}_{t, \mathcal{P}_t}(\mathbf{u}_t) - \hat{C}_{\tau_t^k, \mathcal{P}_t}(\mathbf{u}_{t \rightarrow \tau_t^k})| + |\hat{C}_{t, \mathcal{P}_t}(\mathbf{u}_{\tau_t^k \rightarrow t}) - \hat{C}_{\tau_t^k, \mathcal{P}_t}(\mathbf{u}_{\tau_t^k})|, \quad (11)$$

where  $\hat{C}_{t, \mathcal{P}_t}$  and  $\hat{C}_{\tau_t^k, \mathcal{P}_t}$  denote the rendered frames at training time  $t$  and the latent timestamp  $\tau_t^k$ , respectively, both of which are captured from the same training camera pose  $\mathcal{P}_t$ . Please note that the same camera pose  $\mathcal{P}_t$  is used, resulting in zero warping loss in static regions. This allows the focus to remain on dynamic regions.  $\mathbf{u}_t$  denotes a pixel coordinate in  $\hat{C}_{t, \mathcal{P}_t}$ , while  $\mathbf{u}_{t \rightarrow \tau_t^k}$  represents the corresponding pixel coordinate in  $\hat{C}_{\tau_t^k, \mathcal{P}_t}$ . The transformation of  $\mathbf{u}_t$  to  $\mathbf{u}_{t \rightarrow \tau_t^k}$  is computed as  $\mathbf{u}_{t \rightarrow \tau_t^k} = \mathbf{u}_t + \hat{\mathbf{O}}_{t \rightarrow \tau_t^k}(\mathbf{u}_t)$ , where  $\hat{\mathbf{O}}_{t \rightarrow \tau_t^k}$  denotes the optical flow at pixel  $\mathbf{u}_t$ , estimated from  $\{G_i^{\text{dy}}\}_{i \in [1, n^{\text{dy}}]}$  through the rasterization process, analogous to Eq. 2, as

$$\hat{\mathbf{O}}_{t \rightarrow \tau_t^k}(\mathbf{u}_t) = \sum_{i \in \mathcal{N}} (\mathcal{W}(\mathcal{P}_t, \boldsymbol{\mu}_i(\tau_t^k)) - \mathcal{W}(\mathcal{P}_t, \boldsymbol{\mu}_i(t))) \alpha_i \prod_{j=1}^{i-1} (1 - \alpha_j), \quad (12)$$

where  $\boldsymbol{\mu}_i(t)$  denotes the mean of the  $i^{\text{th}}$  dynamic 3D Gaussian  $G_i^{\text{dy}}$  at time  $t$ . The pixel coordinate  $\mathbf{u}_{\tau_t^k \rightarrow t}$  is computed in the same way as  $\mathbf{u}_{t \rightarrow \tau_t^k}$ . The full optimization objective combines  $\mathcal{L}_{\text{umd}}$ ,  $\mathcal{L}_{\text{tcr}}$ , a depth loss  $\mathcal{L}_{\text{depth}}$ , and a photometric loss  $\mathcal{L}_{\text{rgb}}$ , defined as

$$\mathcal{L}_{\text{total}} = \lambda_{\text{rgb}} \mathcal{L}_{\text{rgb}} + \lambda_d \mathcal{L}_d + \lambda_{\text{umd}} \mathcal{L}_{\text{umd}} + \lambda_{\text{tcr}} \mathcal{L}_{\text{tcr}}, \quad (13)$$

where  $\mathcal{L}_{\text{depth}}$  is an L1 loss between the rendered depth from the rasterization and the ground truth depth, and  $\mathcal{L}_{\text{rgb}}$  is also an L1 loss between the given blurry input frame  $\mathbf{B}_t$  and our rendered blurry frame  $\hat{\mathbf{B}}_t$ .

## 5. Experiments

**Implementation Details.** We refer readers to the supplementary material for the details of our implementation.

**Datasets.** To assess the performance of our MoBGS and other SOTA methods in deblurring dynamic novel view synthesis across various motion blur scenarios, we utilize two datasets: the Stereo Blur dataset [65] and the DAVIS dataset [56]. The Stereo Blur dataset [65] comprises stereo videos of six scenes with significant motion blur, where each scene contains a blurry video from the left view and a corresponding sharp video from the right view. Each video

is captured using a ZED stereo camera at 60 fps. To synthesize blurriness in the left camera, a video frame interpolation (VFI) method [46] is applied to increase the frame rate up to 480 fps, followed by frame averaging, which is used as a common protocol to obtain blurred frames [45, 64]. For each scene, 24 frames are extracted from the original video, and camera parameters are estimated using COLMAP [58] for fair comparison with other methods. We include the DAVIS dataset [56] *for the first time* in deblurring dynamic NVS evaluations. The DAVIS dataset reflects real-world scenarios with diverse scenes featuring rapid camera and object motions, resulting in significant natural real-world blurriness across frames. As reported in [39], COLMAP [58] fails to estimate reliable camera poses for this dataset. To address this, we adopt a more stable method proposed in [71] on camera parameter estimation for ours and all other SOTA methods to do fair performance comparisons. Since the DAVIS dataset does not provide ground truth for NVS, we follow the protocol commonly used in dynamic NVS methods [34, 49] to visualize fixed-view, varying-time renderings for NVS quality assessment.

**Metrics.** For detailed quantitative evaluations, we assess each method using standard image quality metrics, including Peak Signal-to-Noise Ratio (PSNR), Structural Similarity Index Measure (SSIM) [72], and Learned Perceptual Image Patch Similarity (LPIPS) [85], to evaluate the fidelity and perceptual quality of the synthesized novel view frames. To ensure a comprehensive analysis, we compute these metrics over both the entire image region and specifically within the dynamic regions, following the evaluation protocol in [34]. Furthermore, we assess the temporal consistency of the rendered frames by employing tOF [10] which quantifies motion consistency across consecutive frames.

### 5.1. Comparison with State-of-the-Art Methods

The quantitative results for dynamic deblurring NVS on the Stereo Blur dataset [65] are presented in Table 1. As shown in Table 1, the existing dynamic NVS methods suffer from poor perceptual quality and low temporal consistency due to motion blur, as evidenced by higher (worse) LPIPS and tOF scores. This degradation primarily stems from the lack of a dedicated deblurring module, which limits their abilities to effectively reconstruct sharp and temporally coherent novel views. Besides, the static deblurring NVS methods in Table 1 fail to handle scene dynamics effectively. On the other hand, our MoBGS demonstrates *substantial* improvements over the other methods in terms of overall rendering quality, dynamic region reconstruction, and temporal consistency. While the cascade-based approaches in Table 1, which apply 2D deblurring networks as a preprocessing step, offer improvements for the existing dynamic NVS methods, the combination of the two best methods (GShift-Net [32] + SplineGS [49]) still lags behind our MoBGS in

Types	Methods	Full region	Dynamic region only	FPS	Training Time (h)
		PSNR $\uparrow$ / SSIM $\uparrow$ / LPIPS $\downarrow$ / tOF $\downarrow$	PSNR $\uparrow$ / SSIM $\uparrow$ / LPIPS $\downarrow$		
Dynamic NVS	D3DGS (CVPR'24) [81]	15.91 / 0.609 / 0.446 / 6.972	12.74 / 0.301 / 0.556	57	0.30
	4DGS (CVPR'24) [76]	18.53 / 0.710 / 0.270 / 5.400	13.99 / 0.365 / 0.388	193	0.25
	E-D3DGS (ECCV'24) [4]	19.01 / 0.725 / 0.237 / 2.205	15.99 / 0.462 / 0.305	70	2.50
	Shape-of-Motion (arXiv'24) [71]	22.92 / 0.824 / 0.219 / 2.395	15.78 / 0.449 / 0.273	254	1.2
	SplineGS (CVPR'25) [49]	26.41 / 0.902 / 0.141 / 1.409	<u>21.80</u> / 0.756 / 0.177	300	0.25
Cascade (2D Deblurring + Dynamic NVS)	Restormer (CVPR'22) [82] + [4]	18.72 / 0.722 / 0.195 / 2.018	15.72 / 0.452 / 0.261	70	2.50
	GShiftNet (CVPR'23) [32] + [4]	18.85 / 0.721 / 0.189 / 1.627	15.50 / 0.448 / 0.257	76	2.50
	Restormer (CVPR'22) [82] + [71]	22.82 / 0.826 / 0.167 / 2.101	15.72 / 0.444 / 0.238	254	1.2
	GShiftNet (CVPR'23) [32] + [71]	22.62 / 0.824 / 0.158 / 2.070	15.32 / 0.420 / 0.253	254	1.2
	Restormer (CVPR'22) [82] + [49]	<u>26.83</u> / <u>0.914</u> / 0.081 / 0.911	21.76 / <u>0.770</u> / 0.124	<u>336</u>	0.25
Static Deblurring NVS	Deblurring 3DGS (ECCV'24) [26]	15.76 / 0.582 / 0.347 / 3.342	11.34 / 0.236 / 0.482	300	<b>0.18</b>
	BAD-GS (ECCV'24) [86]	21.43 / 0.802 / 0.146 / 1.551	13.81 / 0.350 / 0.353	250	<u>0.2</u>
Dynamic Deblurring NVS	DyBluRF (CVPR'24) [65]	25.62 / 0.895 / 0.079 / 0.889	18.47 / 0.602 / 0.169	0.2	51
	Deblur4DGS (arXiv'24) [77]	23.37 / 0.759 / 0.191 / 1.880	17.48 / 0.543 / 0.307	250	2.4
	<b>MoBGS (Ours)</b>	<b>28.70 / 0.945 / 0.051 / 0.516</b>	<b>22.81 / 0.795 / 0.110</b>	<b>480</b>	1.5

Table 1. **Dynamic deblurring novel view synthesis evaluation on the Stereo Blur dataset.** Red and blue denote the best and second best performances, respectively. Per-scene results are provided in the supplementary material.

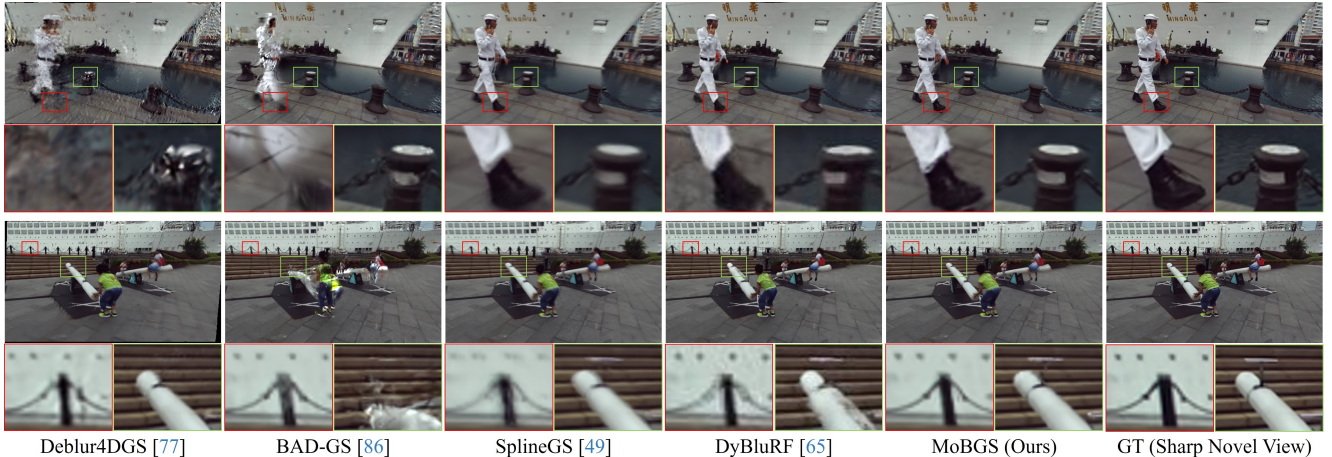


Figure 3. **Visual comparisons for dynamic deblurring novel view synthesis on the Stereo Blur dataset.**

rendering quality. Notably, MoBGS outperforms the latest state-of-the-art (SOTA) dynamic deblurring NVS method, DyBluRF [65], by *very large margins in all metrics*, while achieving *thousands of times* faster rendering speeds and *34 $\times$  faster* training time. Fig. 1, 3 and 4 illustrate the qualitative results on both the Stereo Blur dataset [65] and the real-world videos from the DAVIS dataset [56]. Our visualizations show that MoBGS yields significant improvements in NVS quality, aligning with our quantitative results. Please note that we *first* demonstrate the dynamic deblurring NVS methods on real-world blurry sequences. We provide more visualizations in the supplementary material.

## 5.2. Ablation Study

Our ablation study systematically evaluates the effectiveness of the proposed BLCE and LCEE methods.

**Blur-adaptive Latent Camera Estimation (BLCE).** As

shown in Table 2, removing the deblurring mechanism (i.e., w/o BLCE, w/o LCEE) leads to significantly degraded performance across all metrics, highlighting the adverse effects of blurry training frames. These results underscore the effectiveness of our joint 3D reconstructing and deblurring method for dynamic NVS. To demonstrate the effectiveness of our BLCE method, we replace it with the latent camera pose estimation method from the recent static deblurring NVS approach [27], which does not use the blur feature as input ('w/o blur feature  $\mathcal{B}_t^{k*}$ '). The comparison demonstrates that incorporating  $\mathcal{B}_t^k$  enhances the expressiveness of latent camera estimation, resulting in improved rendering quality. This improvement is reflected by the increase across all metrics, with a particularly notable boost in PSNR. Furthermore, we conduct an ablation study on the number of latent sharp frames ( $N_l$ ) used in our deblurring method. As observed in prior works [25, 70, 86], we



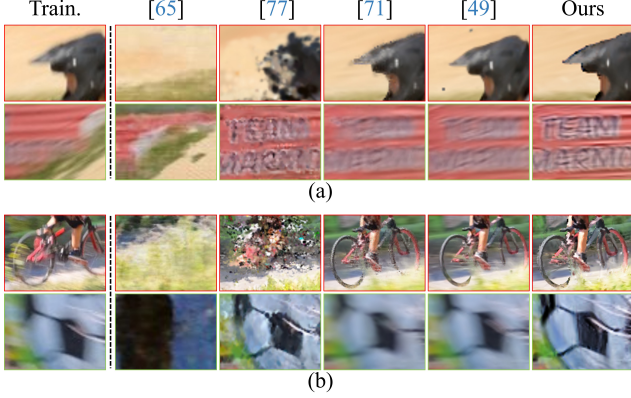


Figure 4. **Visual comparisons for dynamic deblurring novel view synthesis on the DAVIS dataset.** (a) *bmx-bumps* scene. (b) *bmx-trees* scene. ‘Train.’ refers to the training frame. The results of DyBluRF [65] exhibit significant misalignment, as its latent camera pose optimization, based on learnable SE(3) motion bases, is overfitted to the training poses. Full region results are provided in the supplementary material.

Types	Methods	PSNR $\uparrow$	SSIM $\uparrow$	LPIPS $\downarrow$	tOF $\downarrow$
BLCE	w/o BLCE, w/o LCEE	27.67	0.916	0.142	1.326
	w/o blur feature $\mathcal{B}_t^k$	<u>28.36</u>	<u>0.938</u>	<u>0.053</u>	<u>0.539</u>
	<b>Ours</b>	<b>28.70</b>	<b>0.945</b>	<b>0.051</b>	<b>0.516</b>
$N_l$	$N_l = 1$ (Train time: 0.3h)	27.67	0.916	0.142	1.326
	$N_l = 3$ (Train time: 0.8h)	28.28	0.935	0.071	0.671
	$N_l = 5$ (Train time: 1.0h)	28.48	<u>0.940</u>	0.056	0.584
	$N_l = 11$ (Train time: 2.0h)	<b>28.72</b>	<b>0.945</b>	<u>0.052</u>	<u>0.524</u>
	<b>Ours</b> ( $N_l = 9$ ) (Train time: 1.5h)	<u>28.70</u>	<b>0.945</b>	<b>0.051</b>	<b>0.516</b>
LCEE	Fixed $\hat{\mathcal{T}}_t = 0.0$	28.45	0.940	0.059	0.595
	Fixed $\hat{\mathcal{T}}_t = 0.5$ ([65]-like)	<u>28.62</u>	<u>0.943</u>	<u>0.055</u>	<u>0.546</u>
	Fixed $\hat{\mathcal{T}}_t = 0.9$ ([65]-like)	26.42	0.923	0.068	0.759
	Learnable $\hat{\mathcal{T}}_t$ ([77]-like)	28.47	0.939	0.062	0.605
	<b>Ours</b>	<b>28.70</b>	<b>0.945</b>	<b>0.051</b>	<b>0.516</b>

Table 2. **Ablation study conducted on the Stereo Blur dataset.**

observe that increasing  $N_l$  enhances the deblurring effect, particularly improving LPIPS. Our model stabilizes when  $N_l \geq 9$ , leading us to set  $N_l = 9$  as the final configuration for training efficiency.

**Latent Camera-induced Exposure Estimation (LCEE).** Unlike prior works [7, 65, 77], our LCEE introduces a physically-inspired approach to estimating exposure time, ensuring consistent deblurring of both static and dynamic regions. As shown in Fig. 5, an incorrect exposure time setting (e.g.,  $\hat{\mathcal{T}}_t = 0.9$ ) introduces artifacts in dynamic regions, whereas setting  $\hat{\mathcal{T}}_t = 0.0$  fails to account for any motion of dynamic objects, leading to blurry dynamic objects. The adverse effects of incorrect  $\hat{\mathcal{T}}_t$  are also reflected in a worse perceptual score (LPIPS) in Table 2. While a more reasonable but fixed exposure time (e.g.,  $\hat{\mathcal{T}}_t = 0.5$ ) mitigates these artifacts, it remains suboptimal for handling varying

levels of motion blur, requiring manual fine-tuning across different scenarios. Alternatively, treating  $\hat{\mathcal{T}}_t$  as a learnable parameter without any constraints, as in [77], results in inconsistent deblurring between static and dynamic regions. This approach degrades the deblurring effect on moving objects and temporal consistency, as reflected in the metrics of the ‘Learnable  $\hat{\mathcal{T}}_t$ ’ variant in the LCEE section of Table 2, and is further evidenced by the noisy artifacts observed in Fig. 5. Specifically, we further evaluate the robustness of our estimated  $\hat{\mathcal{T}}_t$  by plotting its normalized values alongside the normalization of blur score  $\beta_t$  in Fig. 6. By analyzing the correlation between these values and the corresponding blurry inputs, we observe that  $\hat{\mathcal{T}}_t$  effectively aligns with the degree of blurriness present in the input frames. This strong correlation demonstrates the reliability of our exposure time estimation and its adaptability to varying levels of motion blur, ensuring consistent and robust deblurring performance across different scenarios.



Figure 5. **Visual comparisons for LCEE ablation study.**

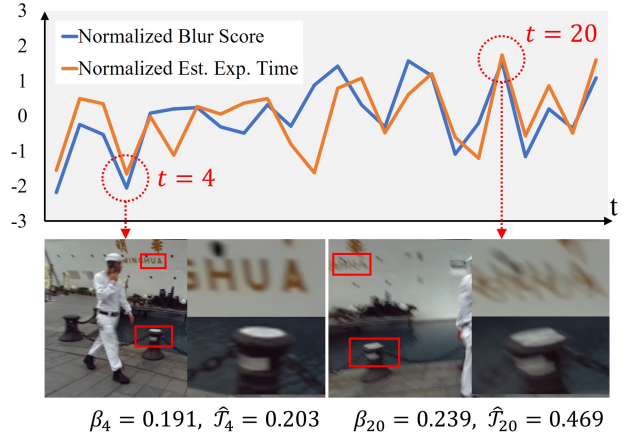


Figure 6. **Correlation between our estimated  $\hat{\mathcal{T}}_t$  (Eq. 9) between our blur score  $\beta_t$  (Eq. 7).** For a clearer comparison of the trend, we normalize  $\beta_t$  and  $\hat{\mathcal{T}}_t$  separately using their respective means and standard deviations for the graph.

## 6. Conclusion

We introduce MoBGS, a novel 3DGS [23]-based dynamic deblurring NVS method for blurry monocular videos. We propose the Blur-adaptive Latent Camera Estimation (BLCE) and Latent Camera-induced Exposure Estimation

(LCEE) methods to accurately model scene blurriness. Experiments on both real-world and synthetic blurry video datasets demonstrate that MoBGS significantly outperforms recent SOTA methods in dynamic deblurring NVS.

## References

- [1] J Harold Ahlberg, Edwin Norman Nilson, and Joseph Leonard Walsh. *The Theory of Splines and Their Applications: Mathematics in Science and Engineering: A Series of Monographs and Textbooks, Vol. 38*. Elsevier, 2016. 3
- [2] ShahRukh Athar, Zexiang Xu, Kalyan Sunkavalli, Eli Shechtman, and Zhixin Shu. Rignerf: Fully controllable neural 3d portraits. In *CVPR*, 2022. 2
- [3] Benjamin Attal, Jia-Bin Huang, Christian Richardt, Michael Zollhoefer, Johannes Kopf, Matthew O’Toole, and Changil Kim. Hyperreel: High-fidelity 6-dof video with ray-conditioned sampling. In *CVPR*, pages 16610–16620, 2023. 1, 2
- [4] Jeongmin Bae, Seoha Kim, Youngsik Yun, Hahyun Lee, Gun Bang, and Youngjung Uh. Per-gaussian embedding-based deformation for deformable 3d gaussian splatting. In *European Conference on Computer Vision*, pages 321–335. Springer, 2024. 1, 3, 7, 5, 6
- [5] Yuval Bahat, Netalee Efrat, and Michal Irani. Non-uniform blind deblurring by reblurring. In *ICCV*, pages 3286–3294, 2017. 2
- [6] Michael Broxton, John Flynn, Ryan Overbeck, Daniel Erickson, Peter Hedman, Matthew Duvall, Jason Dourgarian, Jay Busch, Matt Whalen, and Paul Debevec. Immersive light field video with a layered mesh representation. *ACM Transactions on Graphics (TOG)*, 39(4):86–1, 2020. 1
- [7] Minh-Quan Viet Bui, Jongmin Park, Jihyong Oh, and Munchurl Kim. Dyblurf: Dynamic deblurring neural radiance fields for blurry monocular video. *arXiv preprint arXiv:2312.13528*, 2023. 2, 5, 8
- [8] Ang Cao and Justin Johnson. Hexplane: A fast representation for dynamic scenes. In *CVPR*, pages 130–141, 2023. 2
- [9] Ricky TQ Chen, Yulia Rubanova, Jesse Bettencourt, and David K Duvenaud. Neural ordinary differential equations. *Advances in neural information processing systems*, 31, 2018. 5
- [10] Mengyu Chu, You Xie, Jonas Mayer, Laura Leal-Taixé, and Nils Thuerey. Learning temporal coherence via self-supervision for gan-based video generation. *ACM Transactions on Graphics (TOG)*, 39(4):75–1, 2020. 6
- [11] Wen-Hsuan Chu, Lei Ke, and Katerina Fragkiadaki. Dreamscene4d: Dynamic multi-object scene generation from monocular videos. *arXiv preprint arXiv:2405.02280*, 2024. 2
- [12] Alvaro Collet, Ming Chuang, Pat Sweeney, Don Gillett, Dennis Evseev, David Calabrese, Hugues Hoppe, Adam Kirk, and Steve Sullivan. High-quality streamable free-viewpoint video. *ACM Transactions on Graphics (ToG)*, 34(4):1–13, 2015. 1
- [13] C De Boor. A practical guide to splines. *Springer-Verlag google schola*, 1978. 3
- [14] Carl Doersch, Pauline Luc, Yi Yang, Dilara Gokay, Skanda Koppula, Ankush Gupta, Joseph Heyward, Ignacio Rocco, Ross Goroshin, João Carreira, et al. Bootstap: Bootstrapped training for tracking-any-point. In *Proceedings of the Asian Conference on Computer Vision*, pages 3257–3274, 2024. 1
- [15] Yilun Du, Yanan Zhang, Hong-Xing Yu, Joshua B Tenenbaum, and Jiajun Wu. Neural radiance flow for 4d view synthesis and video processing. In *ICCV*, pages 14304–14314. IEEE Computer Society, 2021. 2
- [16] Yuanxing Duan, Fangyin Wei, Qiyu Dai, Yuhang He, Wenzheng Chen, and Baoquan Chen. 4d-rotor gaussian splatting: towards efficient novel view synthesis for dynamic scenes. In *ACM SIGGRAPH 2024 Conference Papers*, pages 1–11, 2024. 2
- [17] Jiemin Fang, Taoran Yi, Xinggang Wang, Lingxi Xie, Xiaopeng Zhang, Wenyu Liu, Matthias Nießner, and Qi Tian. Fast dynamic radiance fields with time-aware neural voxels. In *SIGGRAPH Asia 2022 Conference Papers*, pages 1–9, 2022. 2
- [18] Sara Fridovich-Keil, Giacomo Meanti, Frederik Rahbæk Warburg, Benjamin Recht, and Angjoo Kanazawa. K-planes: Explicit radiance fields in space, time, and appearance. In *CVPR*, pages 12479–12488, 2023. 1, 2
- [19] Chen Gao, Ayush Saraf, Johannes Kopf, and Jia-Bin Huang. Dynamic view synthesis from dynamic monocular video. In *ICCV*, 2021. 2, 5
- [20] Chen Gao, Ayush Saraf, Johannes Kopf, and Jia-Bin Huang. Dynamic view synthesis from dynamic monocular video. In *ICCV*, 2021. 1
- [21] Yi-Hua Huang, Yang-Tian Sun, Ziyi Yang, Xiaoyang Lyu, Yan-Pei Cao, and Xiaojuan Qi. Sc-gs: Sparse-controlled gaussian splatting for editable dynamic scenes. *CVPR*, 2024. 1, 2
- [22] Wei Jiang, Kwang Moo Yi, Golnoosh Samei, Oncel Tuzel, and Anurag Ranjan. Neuman: Neural human radiance field from a single video. In *ECCV*, 2022. 2
- [23] Bernhard Kerbl, Georgios Kopanas, Thomas Leimkühler, and George Drettakis. 3d gaussian splatting for real-time radiance field rendering. *ACM Trans. Graph.*, 42(4):139–1, 2023. 2, 3, 8, 1
- [24] Byeonghyeon Lee, Howoong Lee, Xiangyu Sun, Usman Ali, and Eunbyung Park. Deblurring 3d gaussian splatting. In *European Conference on Computer Vision*, pages 127–143. Springer, 2024. 2, 3
- [25] Dogyoon Lee, Minhyeok Lee, Chajin Shin, and Sangyoun Lee. Dp-nerf: Deblurred neural radiance field with physical scene priors. In *CVPR*, pages 12386–12396, 2023. 3, 7
- [26] Dongwoo Lee, Jeongtaek Oh, Jaesung Rim, Sunghyun Cho, and Kyoung Mu Lee. Exblurf: Efficient radiance fields for extreme motion blurred images. In *ICCV*, pages 17639–17648, 2023. 3, 7, 5, 6
- [27] Jungho Lee, Donghyeong Kim, Dogyoon Lee, Suhwan Cho, Minhyeok Lee, and Sangyoun Lee. Crim-gs: Continuous rigid motion-aware gaussian splatting from motion-blurred images, 2024. 5, 7

- [28] Jungho Lee, Dogyoon Lee, Minhyeok Lee, Donghyung Kim, and Sangyoun Lee. Smurf: Continuous dynamics for motion-deblurring radiance fields. *arXiv preprint arXiv:2403.07547*, 2024. 2, 3, 5
- [29] Junoh Lee, Chang-Yeon Won, Hyunjun Jung, Inhwan Bae, and Hae-Gon Jeon. Fully explicit dynamic gaussian splatting. In *NeurIPS*, 2024. 2
- [30] Yao-Chih Lee, Zhoutong Zhang, Kevin Blackburn-Matzen, Simon Niklaus, Jianming Zhang, Jia-Bin Huang, and Feng Liu. Fast view synthesis of casual videos with soup-of-planes. In *ECCV*, 2024.
- [31] Jiahui Lei, Yijia Weng, Adam Harley, Leonidas Guibas, and Kostas Daniilidis. Mosca: Dynamic gaussian fusion from casual videos via 4d motion scaffolds. *arXiv*, 2024. 2
- [32] Dasong Li, Xiaoyu Shi, Yi Zhang, Ka Chun Cheung, Simon See, Xiaogang Wang, Hongwei Qin, and Hongsheng Li. A simple baseline for video restoration with grouped spatial-temporal shift. In *Proceedings of the IEEE/CVF Conference on Computer Vision and Pattern Recognition*, pages 9822–9832, 2023. 6, 7, 5
- [33] Tianye Li, Mira Slavcheva, Michael Zollhoefer, Simon Green, Christoph Lassner, Changil Kim, Tanner Schmidt, Steven Lovegrove, Michael Goesele, Richard Newcombe, and Zhaoyang Lv. Neural 3d video synthesis from multi-view video. In *CVPR*, pages 5521–5531, 2022. 2
- [34] Zhengqi Li, Simon Niklaus, Noah Snavely, and Oliver Wang. Neural scene flow fields for space-time view synthesis of dynamic scenes. In *CVPR*, 2021. 2, 5, 6, 1
- [35] Zhengqi Li, Qianqian Wang, Forrester Cole, Richard Tucker, and Noah Snavely. Dynibar: Neural dynamic image-based rendering. In *CVPR*, pages 4273–4284, 2023. 2, 5, 6
- [36] Zhan Li, Zhang Chen, Zhong Li, and Yi Xu. Spacetime gaussian feature splatting for real-time dynamic view synthesis. In *CVPR*, 2024. 2
- [37] Yiqing Liang, Numair Khan, Zhengqin Li, Thu Nguyen-Phuoc, Douglas Lanman, James Tompkin, and Lei Xiao. Gaufré: Gaussian deformation fields for real-time dynamic novel view synthesis. *arXiv*, 2023. 2
- [38] Renting Liu, Zhaorong Li, and Jiaya Jia. Image partial blur detection and classification. In *2008 IEEE conference on computer vision and pattern recognition*, pages 1–8. IEEE, 2008. 5
- [39] Yu-Lun Liu, Chen Gao, Andreas Meuleman, Hung-Yu Tseng, Ayush Saraf, Changil Kim, Yung-Yu Chuang, Johannes Kopf, and Jia-Bin Huang. Robust dynamic radiance fields. In *CVPR*, pages 13–23, 2023. 2, 5, 6, 1
- [40] Jonathon Luiten, Georgios Kopanas, Bastian Leibe, and Deva Ramanan. Dynamic 3d gaussians: Tracking by persistent dynamic view synthesis. In *3DV*, 2024. 2
- [41] Xianrui Luo, Huiqiang Sun, Juewen Peng, and Zhiguo Cao. Dynamic neural radiance field from defocused monocular video. *arXiv preprint arXiv:2407.05586*, 2024. 3
- [42] Achleshwar Luthra, Shiva Souhith Gantha, Xiyun Song, Heather Yu, Zongfang Lin, and Liang Peng. Deblur-nsff: Neural scene flow fields for blurry dynamic scenes. In *Proceedings of the IEEE/CVF Winter Conference on Applications of Computer Vision*, pages 3658–3667, 2024. 3
- [43] Li Ma, Xiaoyu Li, Jing Liao, Qi Zhang, Xuan Wang, Jue Wang, and Pedro V Sander. Deblur-nerf: Neural radiance fields from blurry images. In *CVPR*, pages 12861–12870, 2022. 2, 3
- [44] Ben Mildenhall, Pratul P. Srinivasan, Matthew Tancik, Jonathan T. Barron, Ravi Ramamoorthi, and Ren Ng. Nerf: Representing scenes as neural radiance fields for view synthesis. In *ECCV*, 2020. 2, 3, 5
- [45] Seungjun Nah, Tae Hyun Kim, and Kyoung Mu Lee. Deep multi-scale convolutional neural network for dynamic scene deblurring. In *CVPR*, 2017. 6
- [46] Simon Niklaus, Long Mai, and Feng Liu. Video frame interpolation via adaptive separable convolution. In *Proceedings of the IEEE international conference on computer vision*, pages 261–270, 2017. 6
- [47] Martin Ralf Oswald, Jan Stühmer, and Daniel Cremers. Generalized connectivity constraints for spatio-temporal 3d reconstruction. In *ECCV*, pages 32–46. Springer, 2014. 2
- [48] Jinshan Pan, Deqing Sun, Hanspeter Pfister, and Ming-Hsuan Yang. Blind image deblurring using dark channel prior. In *CVPR*, pages 1628–1636, 2016. 2
- [49] Jongmin Park, Minh-Quan Viet Bui, Juan Luis Gonzalez Bello, Jaeho Moon, Jiyoung Oh, and Munchurl Kim. Splines: Robust motion-adaptive spline for real-time dynamic 3d gaussians from monocular video. *arXiv preprint arXiv:2412.09982*, 2024. 2, 3, 6, 7, 5
- [50] Keunhong Park, Utkarsh Sinha, Jonathan T Barron, Sofien Bouaziz, Dan B Goldman, Steven M Seitz, and Ricardo Martin-Brualla. Nerfies: Deformable neural radiance fields. In *ICCV*, pages 5865–5874, 2021. 2, 5
- [51] Keunhong Park, Utkarsh Sinha, Peter Hedman, Jonathan T. Barron, Sofien Bouaziz, Dan B Goldman, Ricardo Martin-Brualla, and Steven M. Seitz. Hypernerf: A higher-dimensional representation for topologically varying neural radiance fields. *ACM Trans. Graph.*, 40(6), 2021. 2
- [52] Sunghoon Park, Minjung Son, Seokhwan Jang, Young Chun Ahn, Ji-Yeon Kim, and Nahyup Kang. Temporal interpolation is all you need for dynamic neural radiance fields. In *CVPR*, pages 4212–4221, 2023. 2
- [53] Cheng Peng and Rama Chellappa. Pdrf: progressively deblurring radiance field for fast scene reconstruction from blurry images. In *Proceedings of the AAAI Conference on Artificial Intelligence*, pages 2029–2037, 2023. 3
- [54] Cheng Peng, Yutao Tang, Yifan Zhou, Nengyu Wang, Xijun Liu, Deming Li, and Rama Chellappa. Bags: Blur agnostic gaussian splatting through multi-scale kernel modeling. In *European Conference on Computer Vision*, pages 293–310. Springer, 2025. 2, 3
- [55] Luigi Piccinelli, Yung-Hsu Yang, Christos Sakaridis, Mattia Segu, Siyuan Li, Luc Van Gool, and Fisher Yu. Unidepth: Universal monocular metric depth estimation. In *CVPR*, 2024. 1
- [56] Jordi Pont-Tuset, Federico Perazzi, Sergi Caelles, Pablo Arbeláez, Alex Sorkine-Hornung, and Luc Van Gool. The 2017 davis challenge on video object segmentation. *arXiv*, 2018. 1, 2, 6, 7



- [57] Albert Pumarola, Enric Corona, Gerard Pons-Moll, and Francesc Moreno-Noguer. D-nerf: Neural radiance fields for dynamic scenes. In *CVPR*, pages 10318–10327, 2021. 2
- [58] Johannes L Schonberger and Jan-Michael Frahm. Structure-from-motion revisited. In *CVPR*, pages 4104–4113, 2016. 6
- [59] Ruizhi Shao, Zerong Zheng, Hanzhang Tu, Boning Liu, Hongwen Zhang, and Yebin Liu. Tensor4d: Efficient neural 4d decomposition for high-fidelity dynamic reconstruction and rendering. In *CVPR*, pages 16632–16642, 2023. 2
- [60] Jianping Shi, Li Xu, and Jiaya Jia. Discriminative blur detection features. In *Proceedings of the IEEE Conference on Computer Vision and Pattern Recognition*, pages 2965–2972, 2014. 5
- [61] Jianping Shi, Li Xu, and Jiaya Jia. Just noticeable defocus blur detection and estimation. In *Proceedings of the IEEE Conference on Computer Vision and Pattern Recognition*, pages 657–665, 2015. 5
- [62] Liangchen Song, Anpei Chen, Zhong Li, Zhang Chen, Lele Chen, Junsong Yuan, Yi Xu, and Andreas Geiger. Nerf-player: A streamable dynamic scene representation with decomposed neural radiance fields. *IEEE Transactions on Visualization and Computer Graphics*, 29(5):2732–2742, 2023. 2
- [63] Colton Stearns, Adam Harley, Mikaela Uy, Florian Dubost, Federico Tombari, Gordon Wetzstein, and Leonidas Guibas. Dynamic gaussian marbles for novel view synthesis of casual monocular videos. In *SIGGRAPH Asia 2024 Conference Papers*, pages 1–11, 2024. 2
- [64] Shuochen Su, Mauricio Delbracio, Jue Wang, Guillermo Sapiro, Wolfgang Heidrich, and Oliver Wang. Deep video deblurring for hand-held cameras. In *CVPR*, 2017. 6
- [65] Huiqiang Sun, Xingyi Li, Liao Shen, Xinyi Ye, Ke Xian, and Zhiguo Cao. Dyblurf: Dynamic neural radiance fields from blurry monocular video. In *Proceedings of the IEEE/CVF Conference on Computer Vision and Pattern Recognition*, pages 7517–7527, 2024. 1, 2, 3, 5, 6, 7, 8
- [66] Edgar Tretschk, Ayush Tewari, Vladislav Golyanik, Michael Zollhöfer, Christoph Lassner, and Christian Theobalt. Non-rigid neural radiance fields: Reconstruction and novel view synthesis of a dynamic scene from monocular video. In *ICCV*, pages 12959–12970, 2021. 2
- [67] Jack Valmadre and Simon Lucey. General trajectory prior for non-rigid reconstruction. In *2012 IEEE Conference on Computer Vision and Pattern Recognition*, pages 1394–1401. IEEE, 2012. 3
- [68] Basile Van Hoorick, Purva Tendulkar, Didac Suris, Dennis Park, Simon Stent, and Carl Vondrick. Revealing occlusions with 4d neural fields. In *CVPR*, pages 3011–3021, 2022. 2
- [69] Liao Wang, Jiakai Zhang, Xinhang Liu, Fuqiang Zhao, Yanshun Zhang, Yingliang Zhang, Minye Wu, Jingyi Yu, and Lan Xu. Fourier plenotrees for dynamic radiance field rendering in real-time. In *CVPR*, pages 13524–13534, 2022. 2
- [70] Peng Wang, Lingzhe Zhao, Ruijie Ma, and Peidong Liu. Bad-nerf: Bundle adjusted deblur neural radiance fields. In *CVPR*, pages 4170–4179, 2023. 2, 3, 7
- [71] Qianqian Wang, Vickie Ye, Hang Gao, Jake Austin, Zhengqi Li, and Angjoo Kanazawa. Shape of motion: 4d reconstruction from a single video. *arXiv preprint arXiv:2407.13764*, 2024. 2, 3, 5, 6, 7, 1
- [72] Zhou Wang, Alan C Bovik, Hamid R Sheikh, and Eero P Simoncelli. Image quality assessment: from error visibility to structural similarity. *IEEE transactions on image processing*, 13(4):600–612, 2004. 6
- [73] Chung-Yi Weng, Brian Curless, Pratul P Srinivasan, Jonathan T Barron, and Ira Kemelmacher-Shlizerman. Humannerf: Free-viewpoint rendering of moving people from monocular video. In *CVPR*, pages 16210–16220, 2022. 2
- [74] Chung-Yi Weng, Brian Curless, Pratul P. Srinivasan, Jonathan T. Barron, and Ira Kemelmacher-Shlizerman. HumanNeRF: Free-viewpoint rendering of moving people from monocular video. In *CVPR*, pages 16210–16220, 2022. 2
- [75] Guanjun Wu, Taoran Yi, Jiemin Fang, Lingxi Xie, Xiaopeng Zhang, Wei Wei, Wenyu Liu, Qi Tian, and Xinggang Wang. 4d gaussian splatting for real-time dynamic scene rendering. In *CVPR*, 2024. 2
- [76] Guanjun Wu, Taoran Yi, Jiemin Fang, Lingxi Xie, Xiaopeng Zhang, Wei Wei, Wenyu Liu, Qi Tian, and Xinggang Wang. 4d gaussian splatting for real-time dynamic scene rendering. In *CVPR*, 2024. 2, 3, 7, 5, 6
- [77] Renlong Wu, Zhilu Zhang, Mingyang Chen, Xiaopeng Fan, Zifei Yan, and Wangmeng Zuo. Deblur4dgs: 4d gaussian splatting from blurry monocular video. *arXiv preprint arXiv:2412.06424*, 2024. 2, 3, 5, 7, 8, 6
- [78] Wenqi Xian, Jia-Bin Huang, Johannes Kopf, and Changil Kim. Space-time neural irradiance fields for free-viewpoint video. In *CVPR*, pages 9421–9431, 2021. 2
- [79] Ruomei Yan and Ling Shao. Blind image blur estimation via deep learning. *IEEE Transactions on Image Processing*, 25(4):1910–1921, 2016. 5
- [80] Gengshan Yang, Minh Vo, Neverova Natalia, Deva Ramanan, Vedaldi Andrea, and Joo Hanbyul. Banmo: Building animatable 3d neural models from many casual videos. In *CVPR*, 2022. 2
- [81] Ziyi Yang, Xinyu Gao, Wen Zhou, Shaohui Jiao, Yuqing Zhang, and Xiaogang Jin. Deformable 3d gaussians for high-fidelity monocular dynamic scene reconstruction. In *CVPR*, 2024. 2, 3, 7, 5, 6
- [82] Syed Waqas Zamir, Aditya Arora, Salman Khan, Munawar Hayat, Fahad Shahbaz Khan, and Ming-Hsuan Yang. Restormer: Efficient transformer for high-resolution image restoration. In *Proceedings of the IEEE/CVF conference on computer vision and pattern recognition*, pages 5728–5739, 2022. 7, 5, 6
- [83] Kaihao Zhang, Wenhan Luo, Yiran Zhong, Lin Ma, Wei Liu, and Hongdong Li. Adversarial spatio-temporal learning for video deblurring. *IEEE Transactions on Image Processing*, 28(1):291–301, 2018. 2
- [84] Kaihao Zhang, Wenhan Luo, Yiran Zhong, Lin Ma, Bjorn Stenger, Wei Liu, and Hongdong Li. Deblurring by realistic blurring. In *CVPR*, pages 2737–2746, 2020. 2
- [85] Richard Zhang, Phillip Isola, Alexei A Efros, Eli Shechtman, and Oliver Wang. The unreasonable effectiveness of deep

- features as a perceptual metric. In *CVPR*, pages 586–595, 2018. [6](#)
- [86] Lingzhe Zhao, Peng Wang, and Peidong Liu. Bad-gaussians: Bundle adjusted deblur gaussian splatting. In *European Conference on Computer Vision*, pages 233–250. Springer, 2024. [2](#), [3](#), [7](#), [5](#), [6](#)
- [87] Matthias Zwicker, Hanspeter Pfister, Jeroen Van Baar, and Markus Gross. Surface splatting. In *Proceedings of the 28th annual conference on Computer graphics and interactive techniques*, pages 371–378, 2001. [3](#)



# MoBGS: Motion Deblurring Dynamic 3D Gaussian Splatting for Blurry Monocular Video

## Supplementary Material

### A. Implementation details

We build our framework upon the widely adopted open-source 3D Gaussian Splatting (3DGS) codebase [23]. For depth estimation and 2D tracking, we utilize the pre-trained models UniDepth [55] and BootsTAPIR [14], respectively. Our model is trained over 10K iterations, with the LCEE applied after 2K iterations. For each blurry input frame, our BLCE module estimates  $N_l = 9$  latent images. The blur score  $\beta_t$  for the blur feature  $\mathcal{B}_t$  is computed using  $s = 20$ . The loss coefficients are empirically found and set as follows:  $\lambda_{\text{rgb}} = 1.0$ ,  $\lambda_d = 0.2$ ,  $\lambda_{\text{umd}} = 1.0 \times 10^{-7}$ , and  $\lambda_{\text{tcr}} = 1.0 \times 10^{-2}$ . We use  $N_c = 12$  control points for the spline-based motion modeling. Our MoBGS is trained and evaluated on a single NVIDIA RTX 3090Ti.

### B. Demo Videos

We provide an anonymous offline project page, titled ‘MoBGS\_demo.html’, featuring extensive qualitative comparisons of our MoBGS. Since this project page is included as an offline supplementary material, please note that no modifications can be made after submission; it is provided solely for visualization purposes. The project page contains various demo videos, including:

- *Novel View Synthesis Demo* – presenting a comparative analysis of MoBGS against SOTA methods on the Stereo Blur dataset [65], as reported in Table 1.
- *Latent Rendering Demo* – demonstrating the robustness and consistency of our latent image renderings for unseen latent exposure timestamps along the training cameras.

This supplementary resource provides comprehensive visual evidence, further reinforcing the effectiveness of MoBGS in dynamic novel view synthesis under motion blur conditions.

### C. Ablation on Regularizations

Fig. 7 presents the comparisons for the static/dynamic decomposition. Due to the regularization effect of  $\mathcal{L}_{\text{umd}}$ , MoBGS achieves less noisy scene decomposition compared to the variant without  $\mathcal{L}_{\text{umd}}$  (‘w/o  $\mathcal{L}_{\text{umd}}$ ’). Additionally, in contrast to inaccurate preprocessed motion masks obtained by pretrained segmentation and tracking models as proposed in [20, 34, 39, 71], our approach effectively refines the motion mask, particularly ensuring the consistency of motion masks along the temporal axis. Moreover, our MoBGS with  $\mathcal{L}_{\text{tcr}}$  produces consistent renderings at unseen

latent timestamps, ensuring a reliable deblurring process for dynamic objects. For visualization, please check the ‘Latent Rendering Demo’ section of our project page in the supplementary material.

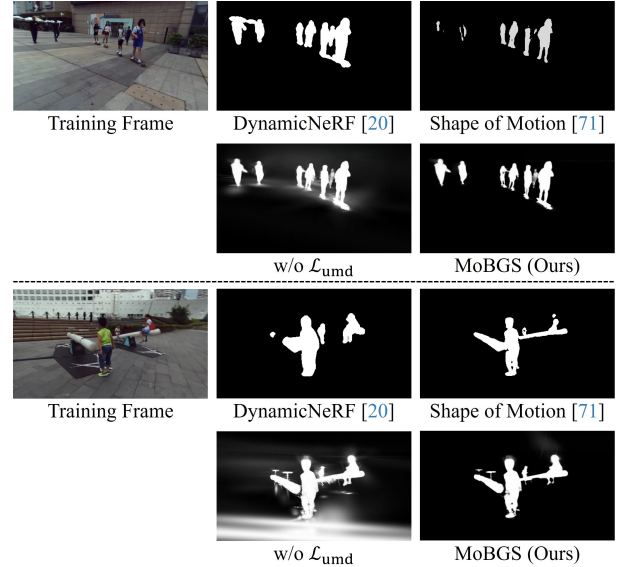


Figure 7. Visual comparisons for scene motion decomposition.

### D. Additional Visual Results on DAVIS dataset

Fig. 8 shows spatio-temporal NVS on the DAVIS dataset. Figs. 9 and 10 present the full-region results of Fig. 4 in the main paper.

### E. Per-scene results on Stereo Blur dataset

In Table 3, 4, 5, 6, 7, 8, 9, we present the detailed quantitative results of all methods reported in Table 1, broken down for each of the six scenes in the Stereo Blur dataset [65]. These tables provide per-scene performance metrics, including PSNR, SSIM, LPIPS, mPSNR, mSSIM, mLPIPS, and tOF, enabling a comprehensive evaluation of the rendering quality, perceptual similarity, and temporal consistency across different methods.





Figure 8. Visual comparisons for dynamic deblurring novel view synthesis on the DAVIS dataset.



Figure 9. Visual comparisons for dynamic deblurring novel view synthesis on the *bmx-bumps* scene from the DAVIS dataset.





Figure 10. Visual comparisons for dynamic deblurring novel view synthesis on the *bmx-trees* scene from the DAVIS dataset.



Types	Methods	Basketball	Children	Sailor	Seesaw	Skating	Street	Average
Dynamic NVS	D3DGS (CVPR'24) [81]	18.74	15.24	12.65	18.49	17.13	13.18	15.91
	4DGS (CVPR'24) [76]	20.75	18.31	14.77	21.65	21.44	14.27	18.53
	E-D3DGS (ECCV'24) [4]	16.67	20.29	17.80	22.14	21.78	15.38	19.01
	Shape-of-Motion (arXiv'24) [71]	23.67	22.07	20.55	22.47	24.39	24.38	22.92
	SplineGS (CVPR'25) [49]	24.98	25.02	24.37	28.09	29.09	26.91	26.41
Cascade (2D Deblurring + Dynamic NVS)	Restormer (CVPR'22) [82] + [4]	16.41	19.67	17.57	22.12	21.55	14.97	18.72
	GShiftNet (CVPR'23) [32] + [4]	16.33	19.76	17.27	22.16	21.82	15.79	18.85
	Restormer (CVPR'22) [82] + [71]	23.73	21.38	20.26	22.90	24.33	24.32	22.82
	GShiftNet (CVPR'23) [32] + [71]	23.62	21.31	20.49	22.80	23.67	23.80	22.62
	Restormer (CVPR'22) [82] + [49]	25.55	25.19	24.84	29.51	29.53	26.38	26.83
Static Deblurring NVS	Deblurring 3DGS (ECCV'24) [26]	17.63	16.75	12.63	18.76	15.31	13.49	15.76
	BAD-GS (ECCV'24) [86]	24.21	21.71	19.19	23.13	22.41	17.95	21.43
Dynamic Deblurring NVS	DyBluRF (CVPR'24) [65]	25.28	25.57	23.50	24.56	27.94	26.88	25.62
	Deblur4DGS (arXiv'24) [77]	23.02	22.10	19.22	23.19	25.97	26.68	23.37
	<b>MoBGS (Ours)</b>	27.39	26.85	27.07	30.62	32.20	28.10	28.70

Table 3. Per-scene PSNR score for dynamic deblurring novel view synthesis evaluation on the Stereo Blur dataset.

Types	Methods	Basketball	Children	Sailor	Seesaw	Skating	Street	Average
Dynamic NVS	D3DGS (CVPR'24) [81]	0.729	0.591	0.472	0.688	0.612	0.561	0.609
	4DGS (CVPR'24) [76]	0.786	0.664	0.574	0.792	0.801	0.641	0.710
	E-D3DGS (ECCV'24) [4]	0.689	0.741	0.666	0.830	0.817	0.606	0.725
	Shape-of-Motion (arXiv'24) [71]	0.874	0.770	0.761	0.832	0.857	0.848	0.824
	SplineGS (CVPR'25) [49]	0.898	0.867	0.861	0.939	0.940	0.907	0.902
Cascade (2D Deblurring + Dynamic NVS)	Restormer (CVPR'22) [82] + [4]	0.678	0.748	0.660	0.828	0.809	0.605	0.722
	GShiftNet (CVPR'23) [32] + [4]	0.684	0.751	0.652	0.829	0.815	0.593	0.721
	Restormer (CVPR'22) [82] + [71]	0.883	0.765	0.754	0.853	0.854	0.846	0.826
	GShiftNet (CVPR'23) [32] + [71]	0.883	0.767	0.769	0.838	0.843	0.843	0.824
	Restormer (CVPR'22) [82] + [49]	0.917	0.888	0.881	0.959	0.947	0.894	0.914
Static Deblurring NVS	Deblurring 3DGS (ECCV'24) [26]	0.720	0.598	0.421	0.738	0.573	0.440	0.582
	BAD-GS (ECCV'24) [86]	0.893	0.817	0.732	0.905	0.819	0.646	0.802
Dynamic Deblurring NVS	DyBluRF (CVPR'24) [65]	0.920	0.884	0.860	0.882	0.917	0.906	0.895
	Deblur4DGS (arXiv'24) [77]	0.815	0.656	0.557	0.781	0.848	0.897	0.759
	<b>MoBGS (Ours)</b>	0.948	0.929	0.924	0.970	0.965	0.932	0.945

Table 4. Per-scene SSIM score for dynamic deblurring novel view synthesis evaluation on the Stereo Blur dataset.

Types	Methods	Basketball	Children	Sailor	Seesaw	Skating	Street	Average
Dynamic NVS	D3DGS (CVPR'24) [81]	0.187	0.490	0.592	0.228	0.560	0.617	0.446
	4DGS (CVPR'24) [76]	0.151	0.315	0.464	0.131	0.186	0.375	0.270
	E-D3DGS (ECCV'24) [4]	0.179	0.267	0.359	0.125	0.166	0.325	0.237
	Shape-of-Motion (arXiv'24) [71]	0.158	0.369	0.306	0.181	0.163	0.139	0.219
	SplineGS (CVPR'25) [49]	0.136	0.243	0.235	0.079	0.080	0.072	0.141
Cascade (2D Deblurring + Dynamic NVS)	Restormer (CVPR'22) [82] + [4]	0.144	0.156	0.299	0.096	0.144	0.333	0.195
	GShiftNet (CVPR'23) [32] + [4]	0.135	0.152	0.305	0.091	0.125	0.326	0.189
	Restormer (CVPR'22) [82] + [71]	0.108	0.248	0.230	0.145	0.147	0.127	0.167
	GShiftNet (CVPR'23) [32] + [71]	0.101	0.230	0.210	0.128	0.145	0.133	0.158
	Restormer (CVPR'22) [82] + [49]	0.078	0.133	0.111	0.046	0.054	0.064	0.081
Static Deblurring NVS	Deblurring 3DGS (ECCV'24) [26]	0.207	0.316	0.496	0.259	0.430	0.372	0.347
	BAD-GS (ECCV'24) [86]	0.085	0.121	0.190	0.075	0.130	0.272	0.146
Dynamic Deblurring NVS	DyBluRF (CVPR'24) [65]	0.050	0.092	0.115	0.075	0.072	0.068	0.079
	Deblur4DGS (arXiv'24) [77]	0.134	0.297	0.352	0.167	0.118	0.078	0.191
	<b>MoBGS (Ours)</b>	0.043	0.064	0.094	0.025	0.034	0.048	0.051

Table 5. Per-scene LPIPS score for dynamic deblurring novel view synthesis evaluation on the Stereo Blur dataset.

Types	Methods	Basketball	Children	Sailor	Seesaw	Skating	Street	Average
Dynamic NVS	D3DGS (CVPR'24) [81]	3.105	12.608	13.189	3.581	6.419	2.929	6.972
	4DGS (CVPR'24) [76]	2.912	12.137	10.357	2.634	2.030	2.329	5.400
	E-D3DGS (ECCV'24) [4]	2.087	4.548	3.378	0.786	0.901	1.528	2.205
	Shape-of-Motion (arXiv'24) [71]	0.726	6.244	3.608	1.550	1.270	0.972	2.395
	SplineGS (CVPR'25) [49]	0.654	4.606	1.697	0.491	0.521	0.482	1.409
Cascade (2D Deblurring + Dynamic NVS)	Restormer (CVPR'22) [82] + [4]	1.991	2.421	4.759	0.604	0.794	1.543	2.018
	GShiftNet (CVPR'23) [32] + [4]	1.795	1.908	3.284	0.597	0.730	1.449	1.627
	Restormer (CVPR'22) [82] + [71]	0.734	5.052	3.367	1.298	1.190	0.965	2.101
	GShiftNet (CVPR'23) [32] + [71]	0.708	5.132	2.855	1.471	1.225	1.031	2.070
	Restormer (CVPR'22) [82] + [49]	0.556	2.417	1.272	0.380	0.367	0.472	0.911
	GShiftNet (CVPR'23) [32] + [49]	0.638	1.531	1.167	0.361	0.350	0.443	0.748
Static Deblurring NVS	Deblurring 3DGS (ECCV'24) [26]	1.103	2.907	6.828	1.703	5.957	1.552	3.342
	BAD-GS (ECCV'24) [86]	0.645	1.486	2.943	0.509	1.620	2.103	1.551
Dynamic Deblurring NVS	DyBluRF (CVPR'24) [65]	0.676	1.460	1.423	0.662	0.592	0.518	0.889
	Deblur4DGS (arXiv'24) [77]	0.592	4.317	4.055	1.045	0.693	0.580	1.880
	<b>MoBGS (Ours)</b>	0.344	0.811	0.941	0.247	0.325	0.427	0.516

Table 6. Per-scene tOF score for dynamic deblurring novel view synthesis evaluation on the Stereo Blur dataset.

Types	Methods	Basketball	Children	Sailor	Seesaw	Skating	Street	Average
Dynamic NVS	D3DGS (CVPR'24) [81]	14.87	10.28	9.39	15.55	12.82	13.55	12.74
	4DGS (CVPR'24) [76]	14.90	12.79	10.08	17.77	14.38	14.05	13.99
	E-D3DGS (ECCV'24) [4]	15.16	16.46	15.55	20.59	14.86	13.35	15.99
	Shape-of-Motion (arXiv'24) [71]	16.12	14.72	13.87	15.89	16.28	17.78	15.78
	SplineGS (CVPR'25) [49]	20.01	19.46	19.77	25.72	23.05	22.82	21.80
Cascade (2D Deblurring + Dynamic NVS)	Restormer (CVPR'22) [82] + [4]	15.15	16.25	15.02	20.65	14.81	12.44	15.72
	GShiftNet (CVPR'23) [32] + [4]	14.71	16.17	13.93	20.32	15.03	12.85	15.50
	Restormer (CVPR'22) [82] + [71]	17.17	14.08	13.29	15.96	16.18	17.63	15.72
	GShiftNet (CVPR'23) [32] + [71]	16.45	13.26	13.59	16.07	15.38	17.17	15.32
	Restormer (CVPR'22) [82] + [49]	19.83	20.29	19.74	25.98	22.58	22.12	21.76
	GShiftNet (CVPR'23) [32] + [49]	19.22	19.96	19.63	26.09	22.02	22.25	21.53
Static Deblurring NVS	Deblurring 3DGS (ECCV'24) [26]	13.18	10.98	8.91	14.54	10.88	9.54	11.34
	BAD-GS (ECCV'24) [86]	16.14	11.45	12.02	15.25	15.29	12.70	13.81
Dynamic Deblurring NVS	DyBluRF (CVPR'24) [65]	18.96	18.16	17.12	16.79	19.43	20.34	18.47
	Deblur4DGS (arXiv'24) [77]	16.71	14.47	15.31	19.29	18.64	20.44	17.48
	<b>MoBGS (Ours)</b>	21.77	19.52	21.61	26.05	26.19	21.69	22.81

Table 7. Per-scene PSNR score of dynamic regions only for dynamic deblurring novel view synthesis evaluation on the Stereo Blur dataset.

Types	Methods	Basketball	Children	Sailor	Seesaw	Skating	Street	Average
Dynamic NVS	D3DGS (CVPR'24) [81]	0.252	0.181	0.259	0.469	0.259	0.387	0.301
	4DGS (CVPR'24) [76]	0.264	0.273	0.294	0.571	0.344	0.441	0.365
	E-D3DGS (ECCV'24) [4]	0.218	0.502	0.509	0.746	0.396	0.400	0.462
	Shape-of-Motion (arXiv'24) [71]	0.404	0.381	0.389	0.424	0.538	0.556	0.449
	SplineGS (CVPR'25) [49]	0.634	0.674	0.701	0.892	0.850	0.783	0.756
Cascade (2D Deblurring + Dynamic NVS)	Restormer (CVPR'22) [82] + [4]	0.211	0.525	0.484	0.751	0.366	0.375	0.452
	GShiftNet (CVPR'23) [32] + [4]	0.195	0.524	0.446	0.736	0.413	0.383	0.449
	Restormer (CVPR'22) [82] + [71]	0.460	0.340	0.356	0.417	0.539	0.554	0.444
	GShiftNet (CVPR'23) [32] + [71]	0.423	0.287	0.366	0.442	0.482	0.519	0.420
	Restormer (CVPR'22) [82] + [49]	0.629	0.755	0.707	0.901	0.847	0.782	0.770
	GShiftNet (CVPR'23) [32] + [49]	0.609	0.733	0.720	0.910	0.835	0.792	0.766
Static Deblurring NVS	Deblurring 3DGS (ECCV'24) [26]	0.208	0.193	0.212	0.411	0.197	0.196	0.236
	BAD-GS (ECCV'24) [86]	0.389	0.175	0.278	0.475	0.448	0.334	0.350
Dynamic Deblurring NVS	DyBluRF (CVPR'24) [65]	0.564	0.625	0.559	0.489	0.663	0.714	0.602
	Deblur4DGS (arXiv'24) [77]	0.407	0.356	0.445	0.708	0.645	0.699	0.543
	<b>MoBGS (Ours)</b>	0.745	0.683	0.759	0.900	0.918	0.765	0.795

Table 8. Per-scene SSIM score of dynamic regions only for dynamic deblurring novel view synthesis evaluation on the Stereo Blur dataset.

Types	Methods	Basketball	Children	Sailor	Seesaw	Skating	Street	Average
Dynamic NVS	D3DGS (CVPR'24) [81]	0.344	0.657	0.700	0.291	0.643	0.703	0.556
	4DGS (CVPR'24) [76]	0.304	0.401	0.575	0.173	0.323	0.553	0.388
	E-D3DGS (ECCV'24) [4]	0.269	0.305	0.396	0.147	0.281	0.432	0.305
	Shape-of-Motion (arXiv'24) [71]	0.302	0.333	0.319	0.219	0.211	0.252	0.273
	SplineGS (CVPR'25) [49]	0.148	0.252	0.280	0.100	0.091	0.189	0.177
Cascade (2D Deblurring + Dynamic NVS)	Restormer (CVPR'22) [82] + [4]	0.245	0.194	0.332	0.127	0.236	0.434	0.261
	GShiftNet (CVPR'23) [32] + [4]	0.221	0.200	0.360	0.112	0.217	0.432	0.257
	Restormer (CVPR'22) [82] + [71]	0.197	0.296	0.291	0.228	0.194	0.222	0.238
	GShiftNet (CVPR'23) [32] + [71]	0.239	0.298	0.262	0.203	0.226	0.288	0.253
	Restormer (CVPR'22) [82] + [49]	0.110	0.160	0.198	0.072	0.063	0.141	0.124
	GShiftNet (CVPR'23) [32] + [49]	0.099	0.157	0.190	0.059	0.063	0.112	0.113
Static Deblurring NVS	Deblurring 3DGS (ECCV'24) [26]	0.379	0.465	0.600	0.356	0.560	0.535	0.482
	BAD-GS (ECCV'24) [86]	0.314	0.384	0.438	0.222	0.284	0.477	0.353
Dynamic Deblurring NVS	DyBluRF (CVPR'24) [65]	0.175	0.188	0.237	0.147	0.117	0.149	0.169
	Deblur4DGS (arXiv'24) [77]	0.275	0.528	0.504	0.168	0.177	0.189	0.307
	<b>MoBGS (Ours)</b>	0.088	0.149	0.195	0.069	0.048	0.109	0.110

Table 9. Per-scene LPIPS score of dynamic regions only for dynamic deblurring novel view synthesis evaluation on the Stereo Blur dataset.